



This is a repository copy of *Dual-laser powder bed fusion using 450 nm diode area melting and 1064 nm galvo-scanning fiber laser sources*.

White Rose Research Online URL for this paper:

<https://eprints.whiterose.ac.uk/220303/>

Version: Published Version

---

**Article:**

Caglar, H. [orcid.org/0009-0001-4800-0064](https://orcid.org/0009-0001-4800-0064), Aydin, A. [orcid.org/0009-0007-3212-8040](https://orcid.org/0009-0007-3212-8040), Gulenc, I.T. [orcid.org/0000-0001-5163-9478](https://orcid.org/0000-0001-5163-9478) et al. (2 more authors) (2024) Dual-laser powder bed fusion using 450 nm diode area melting and 1064 nm galvo-scanning fiber laser sources. *Materials & Design*, 248. 113511. ISSN 0264-1275

<https://doi.org/10.1016/j.matdes.2024.113511>

---

**Reuse**

This article is distributed under the terms of the Creative Commons Attribution (CC BY) licence. This licence allows you to distribute, remix, tweak, and build upon the work, even commercially, as long as you credit the authors for the original work. More information and the full terms of the licence here:

<https://creativecommons.org/licenses/>

**Takedown**

If you consider content in White Rose Research Online to be in breach of UK law, please notify us by emailing [eprints@whiterose.ac.uk](mailto:eprints@whiterose.ac.uk) including the URL of the record and the reason for the withdrawal request.



[eprints@whiterose.ac.uk](mailto:eprints@whiterose.ac.uk)  
<https://eprints.whiterose.ac.uk/>



# Dual-laser powder bed fusion using 450 nm diode area melting and 1064 nm galvo-scanning fiber laser sources

H. Caglar<sup>a,\*</sup>, A. Aydin<sup>a</sup>, I.T. Gulenc<sup>b</sup>, K. Groom<sup>c</sup>, K. Mumtaz<sup>a</sup>

<sup>a</sup> Department of Mechanical Engineering, The University of Sheffield, Sheffield S1 4BJ, United Kingdom

<sup>b</sup> Department of Metallurgical and Materials Engineering, Ankara Yildirim Beyazit University, Ankara, Turkiye

<sup>c</sup> Department of Electronic & Electrical Engineering, The University of Sheffield, Sheffield S1 4BJ, United Kingdom

## ARTICLE INFO

### Keywords:

Multi-laser PBF  
Diode area melting  
450 nm  
Ti6Al4V  
Microstructure control

## ABSTRACT

This study introduces an innovative dual laser powder bed fusion (PBF-LB/D) system, which combines two distinct laser processing methods to enhance control over microstructural outcomes. Unlike conventional PBF-LB systems that employ a single laser type, this dual-laser setup integrates a traversing Diode Area Melting (DAM) laser head with multiple 450 nm diode lasers (4 W each) and a traditional high-power (200 W) 1064 nm fiber-laser. This unique configuration allows for significantly different melt pool solidification rates within the same layer. For the first time, Ti6Al4V feedstock was processed using both laser types within a single sample. A specific scanning strategy defined separate laser processing regions, including an overlap where both lasers interacted to fuse the feedstock and bridge the two regions. The fiber-laser melted (FLM) regions experienced much higher cooling rates ( $\sim 10^7$  °C/s) than the DAM regions ( $\sim 600$  °C/s), resulting in acicular  $\alpha'/\alpha$  phases. In contrast, DAM regions exhibited larger grains, with parent  $\beta$  grain sizes approximately 13 times larger than those in the FLM zone. This dual laser system investigation not only demonstrates microstructural in-situ spatial tailoring but also highlights variations in the laser-induced heat-affected zone, surface roughness, and mechanical properties across different regions within the fabricated Ti6Al4V samples.

## 1. Background

### 1.1. Conventional PBF-LB and diode area melting

Powder Bed Fusion with Laser Beam (PBF-LB) is widely used in the aerospace, automotive, and healthcare industries to produce high-density components [1]. PBF-LB has the advantage of creating customized, geometrically efficient structures with minimal material waste by melting thin layers of metallic feedstock (Ti6Al4V) [1–3]. These conventional industrial-type high power (>100 W) near-infrared (NIR) fiber lasers use a highly focused laser beam (40–100  $\mu\text{m}$  spot diameter) with a galvanometer (galvo) scanner that can reach high scanning speeds (up to 7000 mm/s) and build rates [4–7]. This processing methodology, employing a highly fast moving laser spot leads to a reduced heat-affected zone (HAZ – which is defined as the zone where the material is not melted; however, the microstructure and the mechanical properties are changed due to the heat during the melting) [8,9] and paves the way for the production of high-resolution [10,11]. However, the fast moving laser spot generates a rapid solidification of the melt pool with

cooling rates that can reach  $10^7$  °C/s [12–14]. In the case of Ti6Al4V, a faster cooling rate results in the formation of finer grains (martensite  $\alpha'$ ) within columnar parental  $\beta$  grains, resulting in basket-weave-type anisotropic structures [15]. This also increases the strength and hardness of the material [16]. However, it can also cause an increase in residual stress which can impact dimensional integrity [15,17] and cause intergranular failure [18]. These highly textured structures exhibit substantial variations in mechanical behavior depending on the direction of external forces [19]. Thus, post-heat treatment is generally required to transform martensitic  $\alpha'$  to  $\alpha + \beta$  microstructures not only to enhance mechanical properties but also to reduce residual stress [20]. Xu et al. [20] found that in-situ martensitic decomposition enhanced the total elongation failure to 11.4 % while maintaining yield strength above 1100 MPa of PBF-LB produced as-built Ti6Al4V samples. This was linked to the creation of ultrafine  $\alpha + \beta$  lamellar structures via a change of focal offset distance and energy density (around 50–55  $\text{J}/\text{mm}^3$ ). Aside from rapid melt pool solidification, the highly focused fast moving laser spot can support a reduction in component surface roughness. Dai et al. [21] found that increasing the laser power and scanning speed improved

\* Corresponding author.

E-mail address: [drcaglar.academic@gmail.com](mailto:drcaglar.academic@gmail.com) (H. Caglar).

<https://doi.org/10.1016/j.matdes.2024.113511>

Received 5 July 2024; Received in revised form 3 November 2024; Accepted 28 November 2024

Available online 29 November 2024

0264-1275/© 2024 The Authors. Published by Elsevier Ltd. This is an open access article under the CC BY license (<http://creativecommons.org/licenses/by/4.0/>).

the side surface roughness (SSR) of single fiber laser galvo PBF-LB produced samples (as low as  $R_a$  6.79  $\mu\text{m}$ ). Using a similar approach El Hassanin *et al.* [22] showed that the scanning speed parameter in the contour step significantly affected side surface roughness, with the lowest roughness values achieved at a laser speed of 1200 mm/s.

Diode Area Melting (DAM), an alternative to conventional PBF-LB was developed by investigators at The University of Sheffield [14]. The system integrates multiple low power ( $\sim 4.5$  W) short wavelength (450–808 nm) fiber coupled diode lasers into a laser head that traverse on a gantry system across the powder bed. The diode lasers individually addressable so that each laser can be switched on/off whilst traversing across the powder bed to create net-shape components [14,23,24] see Fig. 1-(A). Each focused laser has a spot size of approximately 100  $\mu\text{m}$  at the substrate. Within the laser head two or more linear arrays of fibers can be tightly packed at a pitch between 75–150  $\mu\text{m}$  to allow suitable beam overlap at the substrate [6,25]. The metal feedstock can be melted more effectively due to the inherently higher laser-absorptivity levels associated with shorter wavelengths. Previous DAM research [7] with Ti6Al4V powder showed that 808 nm diode laser has higher laser absorptivity when compared to a 1064 nm (NIR) laser, followed by a higher absorption rate with the use of a 450 nm laser (Fig. 1-(B)). Due to the use of low powers DAM, the scanning speed of the laser head is much lower than traditional high power fiber galvo-scanning PBF-LB, resulting in a much lower cooling rate,  $\sim 600$   $^{\circ}\text{C}/\text{s}$  when using a 4 W 450 nm diode laser [7]. For Ti6Al4V, a slower cooling rate (below martensitic transition temperature) enables the development of larger grain structures (i.e., equiaxed structure,  $\alpha + \beta$ , or *Widmanstätten*  $\alpha$ ) that assists in the reduction of defect formation [26]. Subsequently, in another study, Alsaddah *et al.* [6] found that martensitic decomposition occurred in certain sections of as-built Ti6Al4V samples with an 808 nm diode laser head within the DAM system. Caglar *et al.* [25] used the DAM approach to process Ti6Al4V using 450 nm laser head within the DAM system. 9 diode lasers (4 W each) in a closely packed linear array within the laser head were used, totaling 36 W of power when all lasers were activated, achieving a part density of 99.3 % and coarser microstructures compared with conventional PBF-LB systems [6,7,25]. Despite DAM's high scalability potential (potentially thousands of lasers within a laser head), the slower DAM scanning speeds create a larger HAZ, reduced resolution capability and rougher size surface roughness compared to conventional PBF-LB systems [6,7,25].

### 1.2. Enhanced melt pool control using dual laser processing methodologies

For Ti6Al4V, the size of parent  $\beta$  grains is determinative for the  $\alpha$  lath size. Heat treatment above  $\beta$ -transus temperature is needed to achieve coarse microstructure [27–29] and the hold time above  $\beta$ -transus

temperature for PBF-LB samples is longer than conventionally PBF-LB manufactured samples [27]. DAM processing as been shown to produce large HAZ, and low cooling rate due to slow scanning speeds [6,25], this can create larger parent  $\beta$  grains compared with traditional PBF-LB and larger  $\alpha$  plates. Some researchers reported that larger parent  $\beta$  grain size and larger  $\alpha$  lath size result in better fatigue properties [30–32]. DAM processing of Ti6Al4V could widen range of material properties using PBF-LB, reduce residual stress and requirement for post-processing. Conventional PBF-LB offers different possibilities in terms of formed microstructures due to rapid cooling rate, a reduced heat effected zone with improved resolution and improved surface roughness compared to DAM. A summary of the two approached based on the laser technology used to process feedstock is summarized in Table 1. In terms of build rate of the both systems, the literature for DAM processing is quite narrow due to technology is being new. In this case, the reported highest build rate for DAM is 0.104  $\text{cm}^3/\text{hr}$  with 9-laser setup [25]. However, it stated that if the number of lasers increased, then build rate will be increased too. For the conventional PBF-LB, it can be said that the theoretical build rate is in between 1.7–16.2  $\text{cm}^3/\text{hr}$  [4–7], however, these build rate can be easily altered with the change of parameters.

In summary, each approach has its own advantages and disadvantages which stem mainly from the distinctly different energy densities and required scanning speeds to achieve complete melting across the powder thickness. By combining both laser processing approaches within the same system there is the potential to harness the advantage of each, including site-specific microstructural tailoring. This develops a novel processing system that incorporates both a high-power fiber galvo-scanning system and DAM 450 nm laser processing head and

**Table 1**

Summary of galvo-scanned NIR fiber laser systems and short-wavelength traverse-scanned diode laser systems from the aforementioned literature.

	Conventional PBF-LB	Diode Area Melting
Wavelength	1060 – 1070 nm	450–808 nm
System Movement Speed	Up to 7000 mm/s	Up to 16.67 mm/s
Power Range	10 – 500 W	Up to 4 W per laser (up to 50 lasers within laser head)
Spot size	40–100 $\mu\text{m}$	72 $\mu\text{m}$ (1 laser only, each laser @ 127 $\mu\text{m}$ pitch from each other)
Ti6Al4V's Absorptivity	58 %	72 %
Scalability Potential	Low	High
Scanning Mechanism	Galvo deflected	Gantry
HAZ & Side Surface Roughness	Low	High

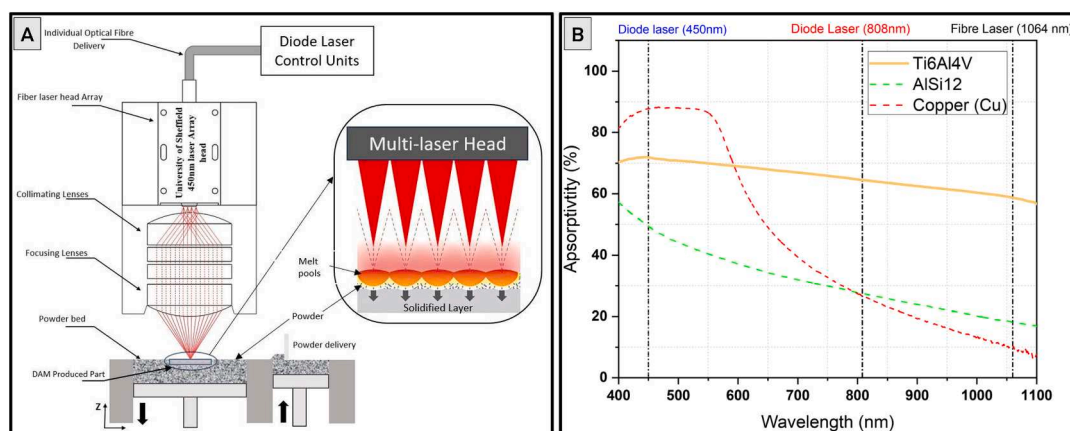


**Fig. 1.** (A) – Operational schematic illustration for diode area melting (Caglar *et al.* [25]), (B) – material's absorptivity percentages at various wavelengths (Alsaddah *et al.* [7]).

explores the potential of using this dual laser PBF technology to create in-situ spatially tailored microstructures within a single Ti6Al4V.

## 2. Methodology

### 2.1. Dual laser beam powder bed fusion system

The dual-laser system developed within this study integrates the strengths of both PBF-LB (galvo and DAM-based) systems. The dual laser system incorporates a galvo-driven 200 W 1064 nm continuous wave solid-state fiber laser alongside a x/y gantry scanning DAM laser head with 9 pieces 4 W 450 nm diode lasers. In this paper, the 1064 nm fiber laser will be referred to as FLM (fiber laser melting), the 450 nm diode multi-laser array system as DAM, and the integrated system PBF-LB/D (powder bed fusion – dual laser beams). Table 2 lists the specifications of these lasers; all lasers have a Gaussian beam profile.

Fig. 2 shows the schematic of the developed bespoke PBF-LB/D system with FLM and DAM laser system. DAM utilizes an x/y gantry system to move the fiber-coupled diode laser head and optics assembly across the processing area (as previously shown in Fig. 1-(A)). The FLM employs a galvo mirror for high-speed scanning with a stationary laser unit fixed above the processing area. After DAM processing the laser head was moved to a location away from the processing area in order not to obstruct FLM processing. A silicone-based wiper blade was used to spread the powder across the substrate [33]. A Crowcon oxygen sensor was used in the build chamber to ensure oxygen content was below 1000 ppm after purging the system with argon. No additional heat sources, such as optical preheating or powder bed heating were used within the build chamber.

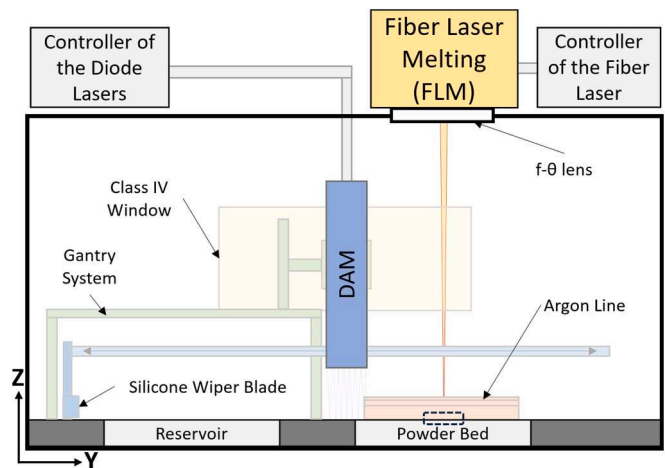
### 2.2. Experimental procedures

Fig. 3 presents a top view schematic of how the two laser sources would scan the powder bed and produce a component. The paths followed by the lasers during the layer processing are shown including an overlap area of approximately 500  $\mu\text{m}$  in width between the lasers. In order, the FLM section was scanned first (pre-FLM, outer left of component), then the DAM section (inner section of component), and finally, the FLM section again (post-FLM). With this approach, the influence of laser technology processing order was investigated within one sample (e.g. influence on degree of melting within the overlap regions based on which laser processing approach was initiated first within the overlap region). Further refinements may be necessary to achieve precise spacing/overlap adjustments.

In the DAM process, the selected processing parameters selected were based upon those optimized for Ti6Al4V within previous DAM 450 nm research [25]. These included a scanning speed of 1.25 mm/s, a hatch distance of 500  $\mu\text{m}$  (when using 9 activated lasers within a linear array), a powder layer height of 60  $\mu\text{m}$ , and a scanning speed of a layer of 4.17 mm/s, resulting in a sample density of 99.3 %, [25]. Moreover, the feature size of a single-track was found as 987  $\pm$  42  $\mu\text{m}$  width. Furthermore, a short preliminary study was undertaken to determine the optimal parameters for FLM laser due to use of the 60  $\mu\text{m}$  layer height. An effective range of 60 to 85  $\text{J}/\text{mm}^3$  of volumetric energy density (VED)

**Table 2**  
Laser equipment specifications employed in the PBF-LB/D system.

Laser system	Fiber Laser Melting	Diode Area Melting
Number of Lasers Used	1	9
Optical Min-Max. Power	20 – 200 W	9 W (1 W x 9) – 36 W (4 W x 9)
System Scan Speed Range	100 – 3000 mm/s	0.16 – 16.67 mm/s
Wavelength	1064 $\pm$ 3 nm	450 $\pm$ 5 nm
Spot Size at FWHM	$\varnothing$ 100 $\mu\text{m}$	659 x 72 ( $\varnothing$ 72 $\mu\text{m}$ per laser)
Focal Length	450 $\pm$ 0.5 mm	60 $\pm$ 1 mm



**Fig. 2.** Custom dual laser beam powder bed fusion (PBF-LB/D) system.

– Equation (1) was found to be necessary based on various studies [1,2,20,34,35].

$$VED = \frac{P}{v \cdot h \cdot t} (\text{J}/\text{mm}^3) \quad (1)$$

where  $P$  is laser power,  $v$  is scanning speed,  $h$  is hatch distance, and  $t$  is layer height. For this setup, it was found that a 80–160 W power range, 500–1500 scan speed range, and 40  $\mu\text{m}$  hatch distance was capable of producing consistent laser tracks on a powder bed. The FLM experiments revealed a standard deviation in density  $\pm$  0.52 %, with a maximum of 99.88 % using 140 W, 900 mm/s, 40  $\mu\text{m}$  hatch distance, 60  $\mu\text{m}$  layer height with a 64.82  $\text{J}/\text{mm}^3$  VED with a single-track width of 63  $\pm$  12  $\mu\text{m}$ .

To ensure the overall consistency of experiments, three nominally identically sized cubes were produced using each laser approach separately and also in combination (dual laser). The measured dimensions of samples were in the range of 5 x 5 mm except for the dual laser samples, in which 500  $\mu\text{m}$  overlapped three cubes in total. The height of all samples was  $\sim$  5 mm (100 layers; the first 15 layers were not considered in any of the calculations as a 66 mm x 66 mm 316L stainless steel substrate was used). Argon gas was purged until the oxygen content was reduced below 0.09 %. The intercooling time between the DAM and FLM procedure is 6  $\pm$  1 s.

The feedstock used in this investigation was a Ti6Al4V Grade 23 PBF-LB supplied by Carpenter Additive, manufactured through gas atomization [36]. The powder has a particle size distribution of 15–45  $\mu\text{m}$  (90 %), with the majority of particles having a sphericity value close to 0.97 (measured). Chemical composition of this feedstock are provided in Table 3.

### 2.3. Analyses procedures

The samples were hot-mounted, a grinding process was carried out, starting with 320 grits and finishing with 4000 grits, followed by polishing using a 0.06  $\mu\text{m}$  colloidal silica solution with 10 %  $\text{H}_2\text{O}_2$ . Densification analyses were conducted across the XZ plane, observed through a Nikon Light Optical Microscope (LOM). Images underwent analysis using ImageJ software to determine density. Following production, samples were placed for 2-minutes in an ultrasonic bath. Alicona Infinite Focus was used to gauge surface roughness, deriving average  $R_a$  values from five distinct graphical measurements. X-Ray Diffraction (XRD) analysis was undertaken using PANalytical Aries, with the start angle set to 30° and ending at 80° with a step size of 0.022 at  $^\circ$ 2 $\theta$ . The scan duration was 10 min. An Oxford Instruments Tescan Vega 3 Scanning Electron Microscope (SEM) was used in both Secondary Electron (SE) and Back Scattered Electron (BSE) modes to capture surface images and

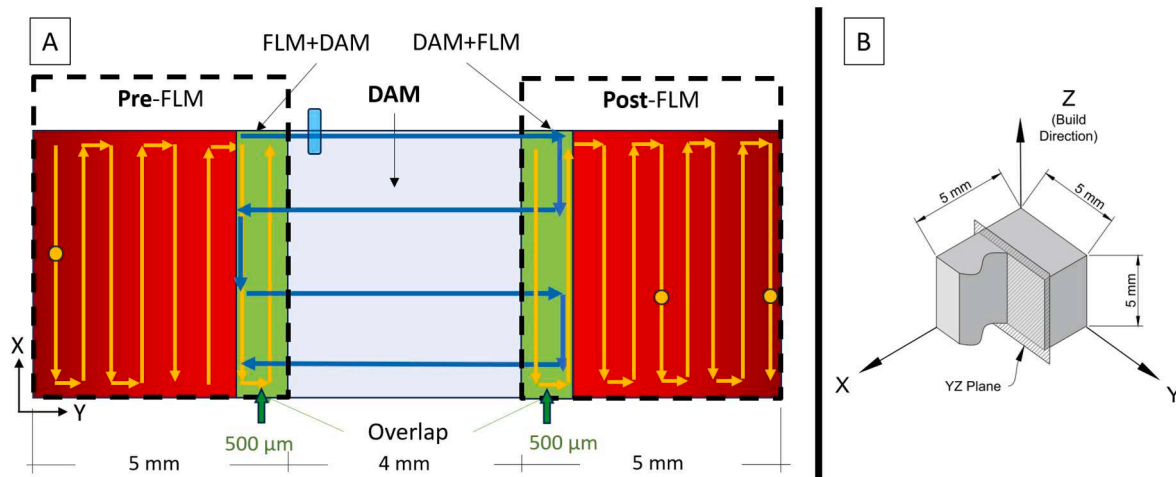


**Fig. 3.** (A) Dual laser scanning segmentation and overlap across sample. Green indicates FLM/DAM laser overlap region ( $\sim 500 \mu\text{m}$  in width). (B) 3D illustration of processed sample for examination axes; Z is the build direction, Y is the scan direction. (For interpretation of the references to color in this figure legend, the reader is referred to the web version of this article.)

**Table 3**  
Ti6Al4V Grade23 alloy specifications.

Chemical Composition [36]									
Element	Ti	Al	V	Fe	O	C	N	H	Y
wt%	Balance	5.5–6.5	3.5–4.5	0.25	0.13	0.08	0.03	0.0125	0.005

reveal the underlying microstructure. The SEM was also fitted with integrated Energy-dispersive X-ray spectroscopy (EDS, EDX, or EDXS) sensors for the purpose of conducting elemental mapping, using AZtec 4.3 acquisition software. During the mapping process, the software analyzed a 1 mm x 1 mm area (with pixel by pixel iterations) and found a uniform distribution without any noticeable peaks or low values. Consequently, error bars are not present in the EDS graphics.

A JEOL-7900F Schottky Field Emission Scanning Electron Microscope was used for Electron Backscatter Diffraction (EBSD) analysis to examine crystallography. The step size was set to 400 nm, and a 0.22 x 2.2 mm<sup>2</sup> area of the YZ plane was scanned. Parent  $\beta$  grains were reconstructed according to Burgers orientation relationship ( $\{0111\}_{\alpha} // \{110\}_{\beta}$  and  $\langle 112^{-}0 \rangle_{\alpha} // \langle 111 \rangle_{\beta}$ ). Aztec Crystal was used to generate pole figures (PF, using an equal area projection, marked with a half-width of 10 degrees, and scaled in multiples of random density), conduct inverse PF (IPF) mapping, parent  $\beta$  grain reconstruction, and grain size analyses. The misorientation limit was set to 10° to identify different sub-grains. Vickers hardness testing was conducted with a 500 g load and a dwell time of 15 s, and three vertical measurements were taken horizontally. Nanoindentation measurements were performed using a 3x3 grid containing 9 points following an open-loop trapezoidal approach during both the loading and unloading phases, utilizing the Micro Materials NanoTest Vantage machine. A brief 5-second pause was included during each stage once the maximum load reached 100 mN. The Young's modulus was calculated from the machine's software, using a Poisson's ratio of 0.342 for the Ti6Al4V Grade 23.

### 3. Results and discussion

#### 3.1. Dual laser processing of multi-layer Ti6Al4V samples

##### 3.1.1. Defining the dual laser scanning order

The sequence by which the scanning strategies are applied to the dual laser sample is an important consideration within this study. This sequence can be either FLM processing first, followed by DAM (FLM + DAM), or DAM processing first, followed by FLM (DAM + FLM). To

investigate the influence of the laser activation sequence on overlap properties and SSR, dual laser samples were produced. These laser scanning sequences (FLM + DAM + FLM) can be seen in Fig. 4-A. Fig. 4-B shows the cross-section of the dual laser sample regions across the YZ plane.

It is evident from Fig. 4-B that the DAM + FLM strategy produces less porosity with a  $98.52 \pm 0.35\%$  density within the overlapped region at the intersection between FLM and DAM processed regions, which exhibits a  $96.09 \pm 0.91\%$  density from three different cross-sections over three samples. These density differences can be explained by the laser-irradiated areas, and the total laser power differences.

In the FLM + DAM strategy, the potential outcome of the intersection being less dense (exhibiting higher levels of porosity) is caused by the DAM system's limited remelting capability. As the DAM initiates scanning from the overlap section, the large spot size focuses on a solid surface. It is well-known that the reflectivity of a solid surface is higher than that of powder feedstock [37]. Consequently, it is likely that the lasers from the DAM system were unable to completely remelt the solidified Ti6Al4V section, resulting in partial connections at the intersection.

On the other hand, in the DAM + FLM strategy, as the powder melts during DAM processing, it leads to a high-sintered powder zone with voids near the edge of the DAM processed section [25]. However, the high power of the fiber laser likely achieved remelting of the solidified overlap section, potentially creating a melt pool track from the solid DAM section towards the FLM section (DAM's HAZ section followed by unprocessed powder) [38]. This is why the intersection area in the DAM + FLM strategy may exhibit a higher density compared to other strategies.

It is significant to note that in the FLM + DAM sections, 3 out of 10 attempts exhibited cracking originating from the intersection region, occurring either during the melting phase or after its completion. This indicates that the FLM + DAM strategy alone does not yield fully reproducible samples at present. The occurrence of cracking can be attributed to residual stresses induced by rapid solidification, given the absence of powder-bed heating. Consequently, when these pre-FLM

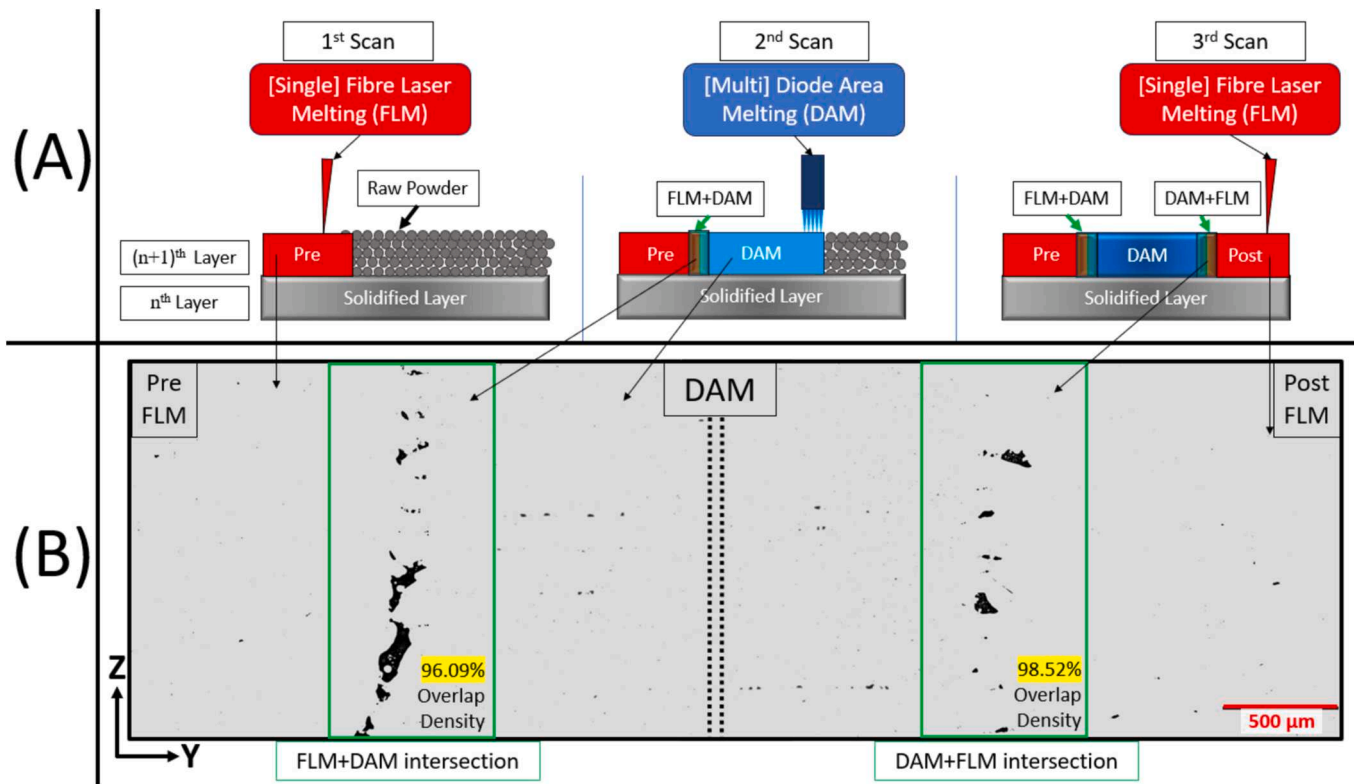


Fig. 4. Scanning order experiments: (a) diagrammatic representation of experiment setup, (b) LOM images adjusted for density analysis with overlap densities. Black points represent porosity.

edge sections merge with the DAM's slow-moving laser track, they may undergo gradual expansion or contraction, leading to cracking or separation.

The SSR of parts was analyzed using dual laser samples in “YZ plane”. It is important to note that the FLM hardware's contouring settings were set to same parameters with the infill parameters, resulting in fixed contouring after infill completion for both pre- and post-FLM parts. The average SSR values were measured in pre-FLM region as  $R_a = 36.5 (\pm 19.9) \mu\text{m}$ , in DAM region as  $R_a = 79.4 (\pm 39.8) \mu\text{m}$ , and in post-FLM region as  $R_a = 15.1 (\pm 7.2) \mu\text{m}$ .

The SSR results of the FLM section are consistent with those described in the literature in terms of values [21,22,39]. We can observe that DAM tends to have a much rougher SSR, almost 100 times more than samples processed by FLM, especially when compared with post-FLM results. This difference can be attributed to the transfer of latent heat when DAM processes are completed. Since DAM is inherently a slow technique, heat builds up during the process, expanding HAZ and allowing more time for heat to conduct into the sides of the melt pool creating a large mass of sintered powder particles that agglomerate to the edge of the melt pool creating a higher side surface roughness [25]. This accumulated heat may function similarly to powder bed heating on the sections that will be processed by post-FLM.

FLM has greatly reduced HAZ and lower side surface finished compared to DAM. FLM could be used to scan the contour of components whilst using DAM to infill portions as an effective solution to address the SSR issue encountered when solely processing using DAM.

### 3.2. Characterization of PBF-LB/D samples

#### 3.2.1. Optical and SEM examination

When examining DAM and FLM samples under a scanning electron microscope (SEM), heavy elements like vanadium (V) and iron (Fe) appear as bright lines and points, while aluminum (Al) appears darker (these elements play a role in stabilizing the  $\beta$  and  $\alpha$  phases, respectively)

[27]. The  $\alpha + \beta$  structure of Ti6Al4V appears with slow cooling rates generally due to a low *in-situ* thermal gradient [12]. LOM (Fig. 5-A-B-C) and SEM/BSE (Fig. 5-D-E-F) images show the cross-section of DAM and FLM processed sections. A higher prevalence of  $\alpha + \beta$  structure can be seen in Fig. 5-A and D. However, parent  $\beta$  grain boundaries were indeterminate in the DAM-processed samples. Conversely, the parent  $\beta$  grain boundaries can be seen in the FLM regions as shown in Fig. 5-C. Moreover, the sub-grain size of the DAM sample (Fig. 5-D) is comparatively much more prominent than that of the FLM sample (Fig. 5-F). The FLM sample exhibits a basket-weave microstructure (Fig. 5-C and F), while DAM exhibits fewer  $\alpha$  laths (Fig. 5-A). This can be attributed to the slower cooling rate in DAM compared to FLM [7,40]. This cooling rate difference allows for the growth of larger sub-grains in DAM, which leads to the formation of  $\alpha + \beta$  grains (Fig. 5-A and D), contrasting with the acicular  $\alpha/\alpha'$  structures observed in FLM (Fig. 5-C and F) [25,41,42]. Fig. 5-B and E shows the overlap area (DAM + FLM), it can be seen that there is a lack of fusion, which has been explained within the dual laser scanning order section. Moreover, the microstructure cannot be seen easily in either of the images within Fig. 5-B and E, especially primary  $\beta$  grain boundaries and sub-grains. To investigate this further EBSD was undertaken to understand the type and size of the laths.

#### 3.2.2. XRD analysis

XRD was used to confirm the presence of different type of phases in the Ti6Al4V samples. In Ti6Al4V phases,  $\alpha$  and  $\alpha'$  possess a Hexagonal Close Packed (HCP) structure, while the  $\beta$  phase has a Body Centered Cubic (BCC) structure. This structural difference results in distinct peak patterns in XRD analyses [41]. The goal was to confirm the presence of the type of structures in Ti6Al4V. The International Centre for Diffraction Data (ICDD) Powder Diffraction File (PDF) cards were used to match the structure of the material with the database. PDF 04-020-7055 [43] card for  $\beta$  phase as this phase cannot be clearly detected at room temperature [26], and 00-044-1294[44] card for  $\alpha$  phase were used to determine the phases of the graph (Fig. 6), which plots the XRD curves

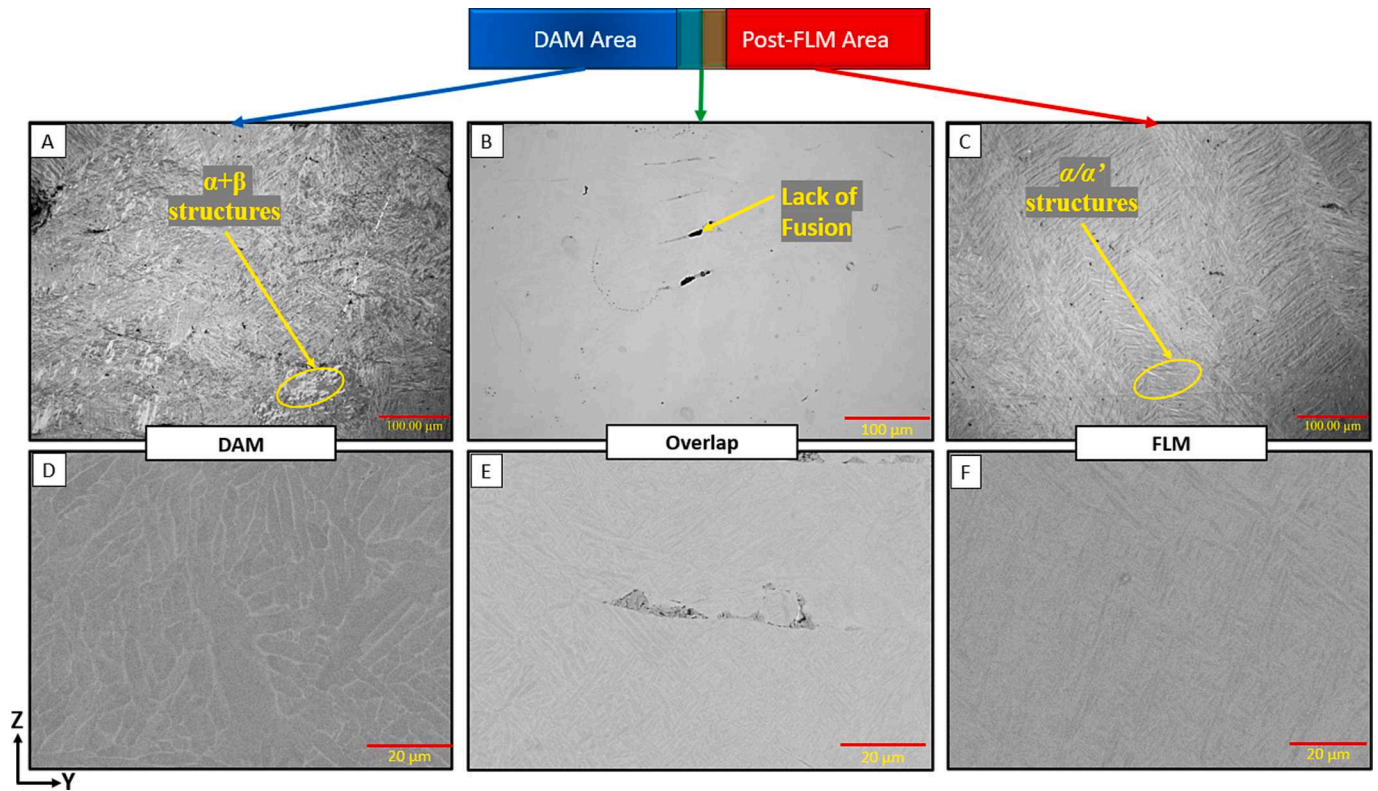


Fig. 5. Microstructure examination through microscopy images at YZ plane cross-section: LOM images of (A) DAM section, (B) overlap section, (C) FLM section, and SEM/BSE images of (D) DAM section, (E) overlap section, (F) FLM section.

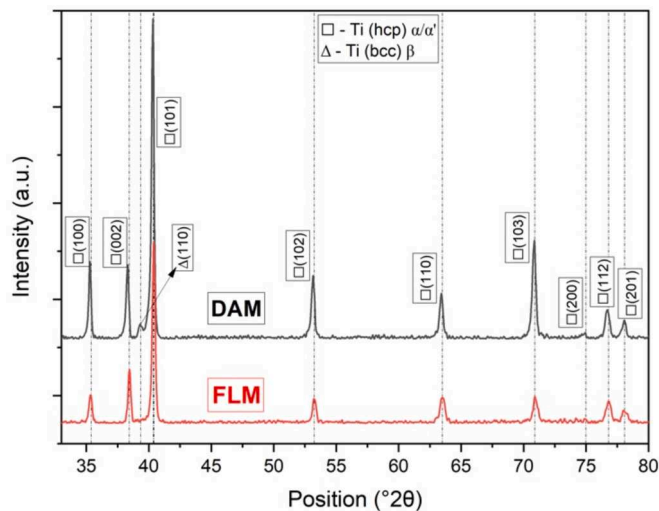


Fig. 6. X-Ray Diffraction patterns of separate DAM and FLM parts: distinct analysis of non-dual laser samples.

obtained for DAM and FLM processed samples. It is evident from these curves that the magnitude of the  $\alpha$  peaks is greater for the DAM samples than for FLM, in their as-built conditions. This correlation can be credited to the larger grain size in DAM, which enables it to reflect more incident beams in a consistent direction toward the collector [41,45]. Additionally, it has been reported that FLM primarily produces  $\alpha'$  structures, characterized by acicular-shaped sub-grains, which may lead to incident beams being less likely to align in the same direction [46]. This phenomenon can be attributed to the slower cooling rate of the DAM process. Furthermore, in the FLM process, a noticeable decrease in peak intensity is observed. This reduction could be attributed to

microstrains caused by dislocations inhibiting sufficient dissolution of the alloy atoms [47,48]. This XRD analysis data was used to set up the EBSD analysis as it determines the phases to be put into the EBSD software.

### 3.2.3. EDS analysis

EDS analyses were conducted in several regions, including the pre- and post- FLM regions, central DAM sections, and the overlap areas in the dual laser samples. The aim of these analyses was to evaluate and compare the degree of elemental loss or vaporization in the various regions, to determine if there were any significant differences. The weight percentage is plotted as a function of position across the sample in Fig. 7 (x-axis not to scale). The color shaded areas represent the acceptable elemental weight percentage range for Ti, Al, V, according to the data sheet [49] and ASTM F1108-97a standard. The amount of oxygen ( $O_2$ ) detected in these analyses was at negligible levels but not perfect zero ( $<0.2\%$ ). This trace  $O_2$  incorporation most likely occurred after the samples were removed from the substrate, as the time prior to measurement could have resulted in surface oxidation. The presence of vaporization would be expected to be in Al due to heat of vaporization being lower than Ti [50,51]. While DAM exhibits a slight tendency towards lower V levels, a potential explanation lies in  $O_2$  content captured as  $V_2O_5$  at elevated temperature [52] which the slower processing speed of the DAM is suitable for this type of oxidation. This suggests that the DAM melt pool exposes the  $O_2$  element more readily than the argon-rich environment of the FLM process. While the slight reduction in V content may not compromise the alloy's mechanical properties, it underscores the necessity for careful optimization of the DAM process to ensure continued safety and performance.

### 3.2.4. EBSD analysis

EBSD analysis was focused on a sample section processed with DAM + FLM to reveal the crystallographic and microstructural changes as the samples transition between the DAM and FLM processed zones. The

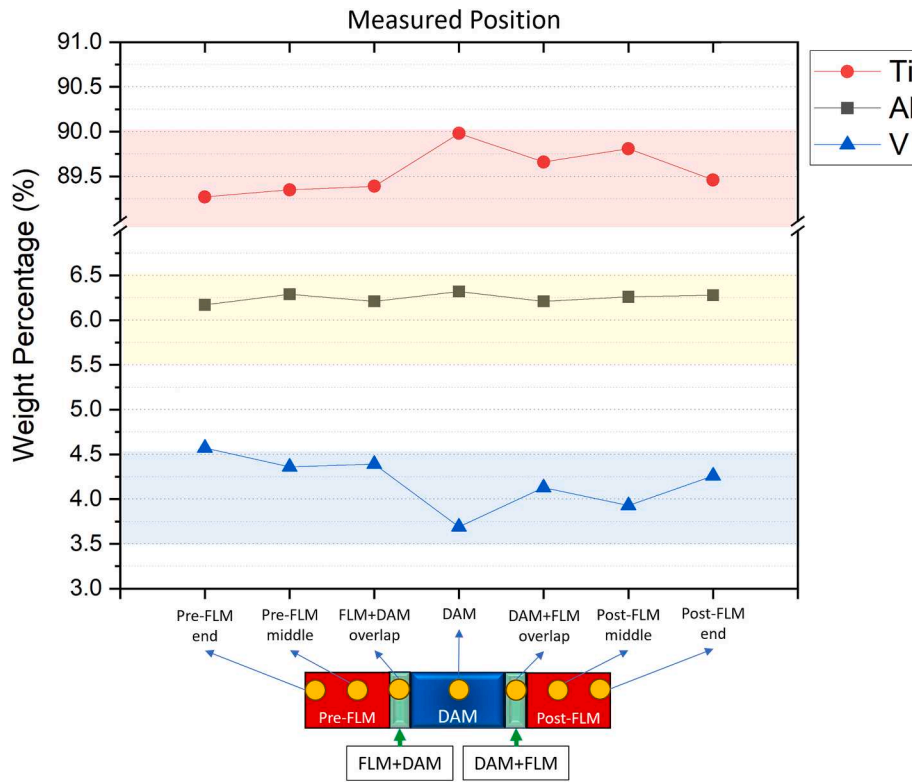


Fig. 7. Locations and elemental percentages in EDS mapping: Averaged area values, indicated by yellow circles (not to scale), were obtained from the FLM section at the center of the individually processed area and the exact midpoint between the first center and the overlap area. In the overlap area, the center was analyzed. For DAM, the center was also selected. These areas represent acceptable ranges of elements in Ti6Al4V according to ASTM F1108-97a and datasheet [49]: red for Ti, yellow for Al, and blue for V. (For interpretation of the references to color in this figure legend, the reader is referred to the web version of this article.)

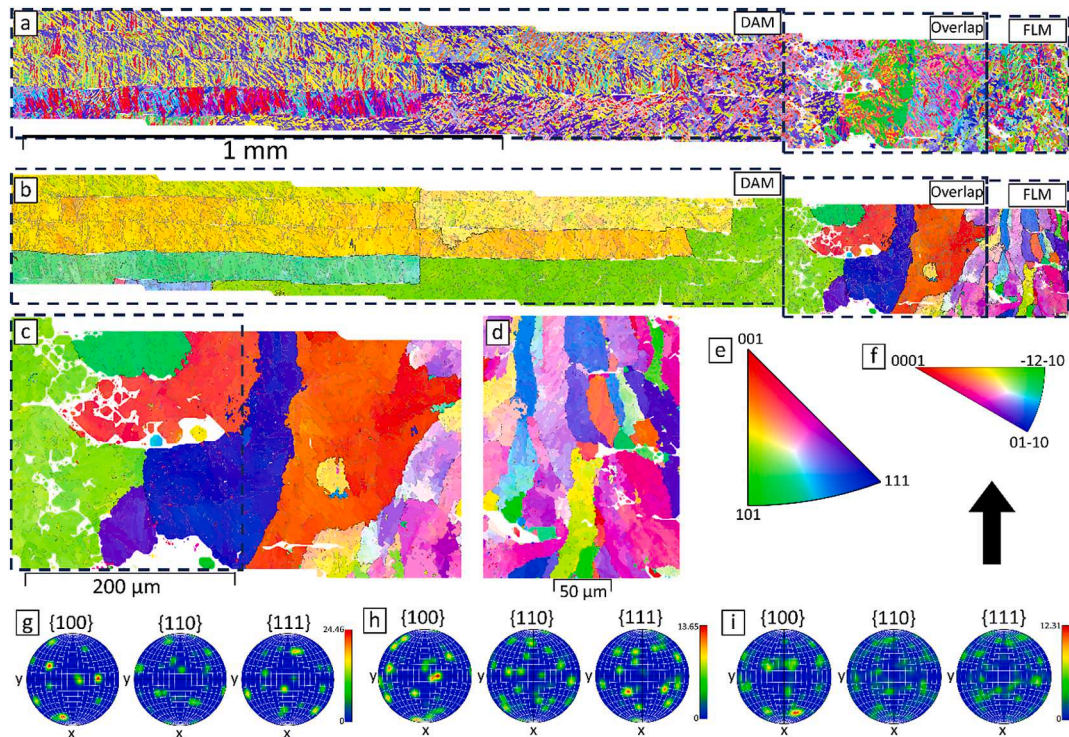


Fig. 8. Dual-laser processed sample (DAM + FLM section only) IPFs: (a)  $\alpha$  phase, (b) reconstructed parent  $\beta$  grains and, DAM, transition and FLM zones, magnified views of (c) transition and (d) FLM zones, color key for (e)  $\alpha$  phase and (f)  $\beta$  phase, pole figures of reconstructed parent  $\beta$  grains' from (g) DAM, (h) overlap and (i) FLM zones. IPFs colors in (a)-(d) are represented according to Z axis (build direction, shown at the bottom right arrow).

EBSDB results are shown in Fig. 8, which shows the complete scan of three divided zones to distinguish the DAM, DAM + FLM (overlapped), and FLM processed regions. IPF colorings are represented in the build direction. The IPF of the original scan is provided in Fig. 8-a. The maximum feret diameter is used to evaluate the size of  $\alpha/\alpha'$  laths in the different zones. The average maximum Feret diameter for DAM, overlapped, and FLM zones are measured as 6.85  $\mu\text{m}$ , 7.1  $\mu\text{m}$  and 6.61  $\mu\text{m}$ , respectively. Thus, the  $\alpha$  laths are 7 % larger in the overlapped region than they are in the FLM region, and only 3 % larger than in the DAM region. Despite detection of the  $\beta$  phase in XRD analysis (Fig. 6), the amount of  $\beta$  detected by EBSD is less than 0.5 % in volume in all three zones.

The IPF of parent  $\beta$  grains reconstructed from Fig. 8-a according to the Burgers orientation relationship is given in Fig. 8-b. The DAM, overlapped, and FLM processed zones are again identified with the dashed rectangles. The grain area is used to evaluate parent  $\beta$  grain size, as parent  $\beta$  grains are much larger than  $\alpha$  laths. The average grain area was measured as 5940  $\mu\text{m}^2$  for DAM, 590  $\mu\text{m}^2$  for overlap and 454  $\mu\text{m}^2$  for FLM regions. This indicates that parent  $\beta$  grains in the DAM zone are approximately x10 larger than in the overlap zone and 13 times larger than in the FLM zone. None of the parent  $\beta$  grains imaged in the DAM zone were scanned completely. This indicates that the DAM grains are even larger than the calculated numbers.

Magnified views of overlapped and FLM zones are shown in Fig. 8-c-d for clarity. Different parent  $\beta$  grain structures can be seen in the different zones in Fig. 8-b-c-d. The DAM region exhibits large and wide grains (Fig. 8-b, DAM) with all grains larger than the EBSD imaging size despite the millimeter scale image. In contrast, the overlapped and FLM regions (Fig. 8-c-d) exhibit much smaller parent  $\beta$  grains. Parent  $\beta$  grains of the transition zone started to follow the grains of the DAM zone (Fig. 8-b, DAM zone, and Fig. 8-c, dashed rectangle) and transform into columnar grains as the distance from the DAM zone increases. In the FLM zone (Fig. 8-d), the grains are completely transformed into columnar grains; however, these grains are noted to be of smaller size than in the overlapped zone.

Pole Figures for reconstructed grains in DAM, overlapping and FLM zones are given in Fig. 8-g-h-i, respectively. A texture is noted in certain areas within the DAM zone (Fig. 8-g). However, this texture mostly arises due to the presence of large parent  $\beta$  grains. A weak texture in the  $\langle 100 \rangle_{\beta}$  direction is observed for the overlapping zone (Fig. 8-h). Two relatively large grains, colored in red in overlapped zone (Fig. 8-c), result in this texture, though other randomly distributed smaller grains cause a spread texture. The FLM zone (Fig. 8-i) does not have a strong texture and grains are mostly distributed in random directions relative to the build direction.

Parent  $\beta$  grains are the first to solidify upon cooling of the melt pool. Therefore, parent  $\beta$  grains could potentially give useful information about the solidification characteristics of DAM, overlap, and FLM zones. This provides a larger liquid volume and cooling rate in the DAM zone ( $\sim 600^\circ\text{C/s}$  [6]) which is much slower than FLM cooling rate ( $\sim 10^7^\circ\text{C/s}$  [42,53]) due to this wide molten metal volume of DAM ( $>1000 \mu\text{m}$  [25]). Hence, much larger parent  $\beta$  grains in millimeter scale were formed due to large molten volume and lower cooling rate. Upon cooling down further, the parent  $\beta$  grain microstructure transformed into  $\alpha + \beta$  microstructure. However, this cooling rate may still not be low enough for the formation of coarse  $\beta$  grains. Ahmed and Rack [26] suggested that the critical cooling rate for martensitic transformation is  $410^\circ\text{C/s}$ . The cooling rate for DAM measured by Alsaddah et al. [6,7] is  $\sim 600^\circ\text{C/s}$  when using 808 nm diode lasers (50 W and double array of 5 lasers). This is close to the critical cooling rate for martensitic formation and is the likely cause of formation of fine  $\beta$  grains distributed within the  $\alpha$  matrix. Considering the 400 nm step size of the EBSD scan, fine  $\beta$  grains would be undetectable with EBSD.

The overlapping can be confirmed via microstructural changes (Fig. 8-a-b). The DAM system traverses and melts the layer prior to scanning with the FLM laser. Therefore, in the overlapped region, FLM

re-melts a solid layer rather than the powdered layer. Columnar grains are formed in the PBF process, and these columnar grains grow through many layers [16,54]. Similar to this mechanism, grains in the overlapping region grow from previous solid DAM parent  $\beta$  grains (Fig. 8-c), dashed rectangle. As the parent grains are wide large grains in the DAM zone, the grains within the overlapping zone follow their direction due to their growth from these parent grains. However, these grains subsequently transform into vertical columnar grains as the distance from the DAM region is increased due to heat transfer through the substrate [16]. This creates different granular directions within the overlap zone.

The FLM zone contains the smallest parent  $\beta$  grains compared to the two other zones (Fig. 8-d). All these grains are columnar with a vertical growth direction. This is expected for the PBF-LB process [16,54] which typically uses fiber lasers similar to the one used in processing the FLM zone in this study. A smaller melt pool and a faster cooling rate in the FLM zone resulted in smaller parent  $\beta$  grains and the transformation from the large wide parent grains in the DAM zone to the smaller vertical parent grains in the FLM zone can be identified within the overlap zone (Fig. 8-c).

The overlapped region provided the largest  $\alpha$  lath size compared to the DAM and FLM zones. The FLM zone has the smallest  $\alpha$  lath size, which is an expected consequence of the rapid cooling rate. It is followed by the DAM and the overlapping regions, respectively. It is likely that remelting within the overlap region provided the highest energy input, resulting in this region exhibiting the highest  $\alpha$  lath size. Additionally, the larger parent  $\beta$  grain size of the DAM region is the reason behind the larger  $\alpha$  size as parent  $\beta$  grain size determines  $\alpha$  lath size. The larger  $\alpha$  lath size of DAM region could provide better fatigue properties for DAM processed alloy. Various researchers reported that fatigue resistance of larger  $\alpha$  lath size is desirable for better fatigue properties [30–32]. The coarser grains for DAM could provide better fatigue resistance in as-built microstructure compared to conventional PBF-LB. This suggests that despite the cooling rate being sufficiently low to obtain a detectable  $\beta$  phase by XRD, the cooling rate was still not low enough to generate  $\beta$  grains large enough to be detected by EBSD. This could explain why the  $\beta$  volume fraction was below 0.5 %.

Three different microstructures in FLM, DAM, and overlapping zones can be detected in Fig. 8. This indicates that the dual laser PBF method can generate variable microstructures, with capability for site-specific microstructural manipulation.

### 3.2.5. Micro and Nano-Indentation

The micro-hardness data presented in Fig. 9 indicate that the

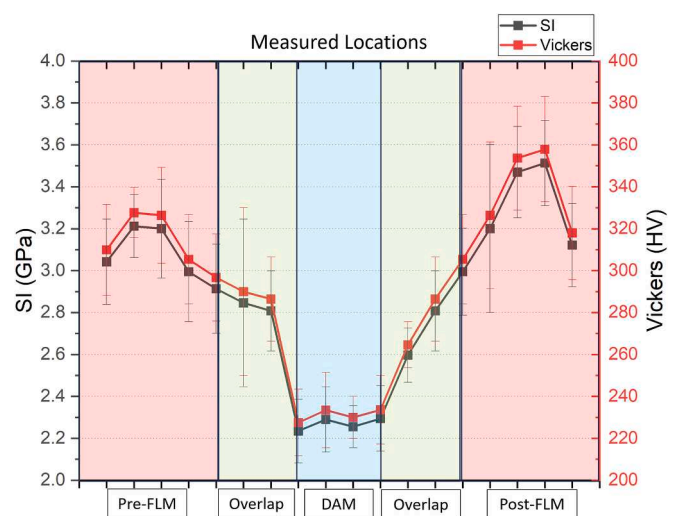


Fig. 9. Micro-Vickers hardness test results for the FLM + DAM + FLM configuration. Locations were spaced 200  $\mu\text{m}$  apart, except in the DAM region, where they were 1 mm apart.

material has softer characteristics during the DAM phase, with increasing hardness observed in the FLM phase. The Hall-Petch relationship suggests that a fine microstructure increases the hardness of the material, as reported in the literature [55,56]. Specifically, the FLM-processed material exhibits hardness values ranging from 3.0 to 3.4 GPa, in contrast to the 2.2 to 2.3 GPa range for the DAM-processed section. These findings align with the EBSD analysis, which shows that a coarser microstructure of Ti6Al4V contributes to reduced hardness. The data collected indicates that the pre-FLM section experienced lower levels of hardness relative to the post-FLM section. The variance in hardness can be attributed to increased heat exposure (in FLM + DAM) resulting from the DAM process as explained in the scanning strategy section. Conversely, the post-FLM section demonstrated higher Vickers hardness values related to the rapid cooling rate inherent to the process. Moreover, the microstructure at the DAM overlap appears to undergo changes in the post-FLM section, leading to an increase in post-FLM hardness values when compared to pre-FLM values.

This may be attributed to two potential factors; firstly, it is the DAM's retraction delay time, which is necessary for FLM initiation. This delay may decrease the overall temperature of the powder bed leading to a high temperature gradient for FLM processing. Secondly, the FLM functions in a way to a remelting over the transition area, but at a much higher speed. This accelerated process results in more refined microstructures compared to those found in the DAM-processed area. Overall, both are related to high cooling rate caused by FLM which created finer

microstructures.

Accurate micro-hardness measurement can be challenging due to the large indentation area. Any air gap between the specimen and the hot-mounted bakelite structure can have a similar effect to that of a spring, reducing the measured hardness. A similar effect on the results can also be caused by a high level of porosity beneath the indentation surface (especially at the overlap region in this sample), as this will create deformation to the material. Nano-indentation has a much smaller indenter inherently, therefore, expected to nano-scale measurements due to the much smaller impact area of the indenter compared to micro-hardness. Fig. 10 displays a load and depth graph under a maximal load of 100 mN of the results of the nano-indentation hardness analyses for the as-built Ti6Al4V specimens (FLM + DAM + FLM). It illustrates the reduced modulus of elasticity, calculated Young's modulus, and the hardness values across nine distinct matrix locations within the sample.

The results are consistent with the micro-indentation hardness data in most regions, apart from the section which was processed with DAM. The cause of the reduced hardness seen in the DAM area might be the presence of nano-porosity between the layers, which could negatively impact the nano-hardness measurements and potentially result in lower hardness values. This can be seen in load cycles data in location 8 in pre-FLM region in Fig. 10 as the hardness measurements shifted. This explanation could also apply to the overlap area, where some degree of porosity has been documented. Hence, the occurrence of porosity in

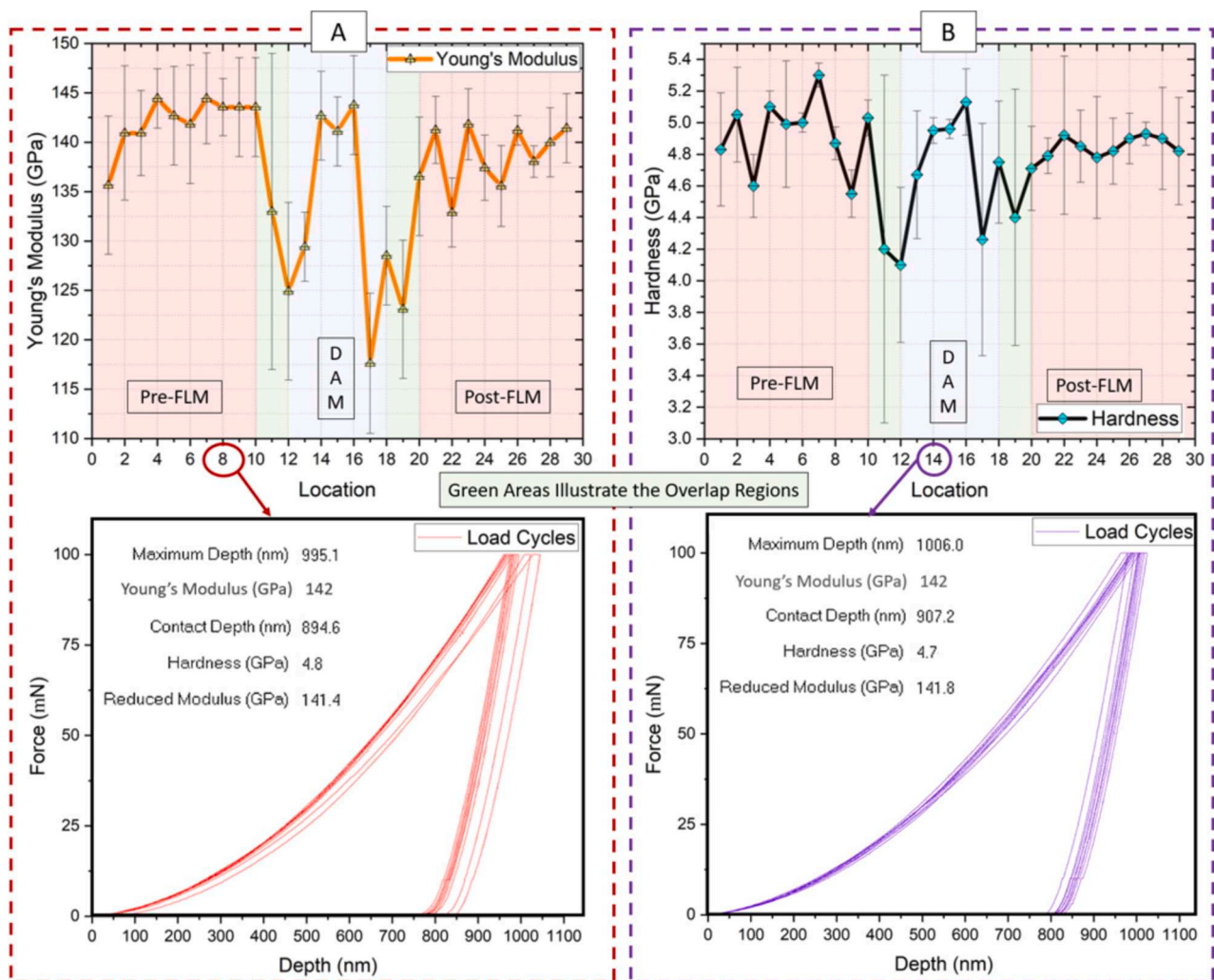


**Fig. 10.** Nano-Indentation test results for FLM + DAM + FLM sample spanning Pre-FLM to Post-FLM: (A) Young's modulus measurements, (B) hardness evaluations, including overlap and DAM-only regions. Locations were spaced 200 μm apart, except in the DAM region, where they were 1 mm apart.

these regions could account for the discrepancies in the outcomes, as highlighted by the large error bars in the data.

Nano-indentation appears to provide a more accurate measure of the hardness of certain phase structures [6], as it is unaffected by potential sub-surface processing or material preparation defects, ensuring an accurate measurement of the hardness of, for instance, martensite  $\alpha'$  structures. Variations in hardness can be accounted for by the indenter impacting different phases, such as  $\alpha'$ ,  $\alpha + \beta$ , or  $\beta$ , with  $\alpha'$  exhibiting higher levels of hardness in most cases [12,27,41]. Compared to the post-FLM and DAM areas, the EBSD data showed larger sub-grain sizes in the overlap regions. According to the Hall-Petch relationship [47,48,57–61], this implies a lower level of hardness at these interfaces, as can be seen in Fig. 10. In addition, there was an apparent increase in both Young's modulus and hardness as the cooling rate decreased. In this context, the scanning speed of the DAM is significantly lower than that of a FLM, 1.25 mm/s and 900 mm/s respectively, which has an impact on the cooling dynamics and the resultant microstructure/mechanical properties.

Generally, post-process heat treatment is required to achieve  $\alpha + \beta$  structures or highly elevated in-situ powder-bed temperatures such as those experienced within the EBM process (above 600°C) [35]. Moreover,  $\alpha + \beta$  structures generally exhibit a better ductility and more favorable total elongation failure in the industry [20,35]. These hardness results may indicate that the ductility of the DAM processed area ( $\alpha + \beta$ ) is higher than that of a FLM processed area (acicular  $\alpha'$ ), which can eliminate the necessity for post-heat treatment procedure [20,35]. This dual-laser approach implemented in this study generates a wider range of melt pool solidification rates and sizes than conventional PBF-LB. When used strategically, this method can provide a viable methodology for spatially tailoring a material's microstructure, enabling the manipulation of its mechanical properties and enhancement of its performance beyond that attainable with current state-of-the-art techniques.

#### 4. Conclusion

In this study, a dual PBF-LB system combining a closely packed linear array of 450 nm diode lasers together with a 1064 nm fiber laser was used to process Ti6Al4V feedstock. It was found that there was a variation in sample properties (microstructure, mechanical properties, and surface roughness) across the FLM, DAM, and laser overlap regions. EBSD data showed significant grain size differences: DAM sections possessed larger parent grains almost 13 wider than fiber laser processed sections. These differences were related to the vastly different cooling rates generated by each laser processing methodology. Larger sub-grain sizes were observed at the overlap of the dual sample, which linked to a rescanning effect by the FLM. It was unclear whether the fiber laser actively remelted the overlap areas or whether the effects were solely due to active or latent heat transfer. The process resulted in significant hardness variations within the overlap area due to low density. Also grain size was correlating with the Hall-Petch relationship while displaying more ductile properties within the DAM section (mainly  $\alpha + \beta$  structures) and less ductile within the FLM section (mainly acicular  $\alpha'$ ). Generally, superior ductility and total elongation failure characteristics are associated with  $\alpha + \beta$  structures. Achieving these structures typically requires post-process heat treatment or elevated powder-bed temperatures, typically those seen within EBM. This implies the possibility of eliminating post-heat treatment within traditional PBF-LB if coupled with the DAM laser processing approach. The dual laser coupling approach implemented within this study creates a range of melt pool solidification rates and melt pool sizes that extend beyond that capable of conventional PBF-LB. When used strategically this approach can provide a viable methodology for spatial tailoring of a material's microstructure, consequently enabling the manipulation of its mechanical properties and enhancing its performance beyond that which is possible with current state-of-the-art.

#### Declaration of generative AI and AI-assisted technologies in the writing process

During the preparation of this work the author(s) used 'GrammarlyPro' to check grammar mistakes. After using this tool/service, the author(s) reviewed and edited the content as needed and take(s) full responsibility for the content of the publication.

#### CRediT authorship contribution statement

**H. Caglar:** Writing – review & editing, Writing – original draft, Visualization, Validation, Methodology, Investigation, Formal analysis, Conceptualization. **A. Aydin:** Visualization, Formal analysis. **I.T. Gulenc:** Writing – review & editing, Visualization, Validation, Software, Formal analysis, Data curation. **K. Groom:** Supervision, Conceptualization. **K. Mumtaz:** Writing – review & editing, Supervision, Methodology, Conceptualization.

#### Declaration of competing interest

The authors declare that they have no known competing financial interests or personal relationships that could have appeared to influence the work reported in this paper.

#### Acknowledgment

This study was completed with support from the Turkish Government Ministry of Education and EPSRC (EP/P006566/1 and EP/W024764/1).

#### Data availability

Data will be made available on request.

#### References

- [1] H. Shipley, D. McDonnell, M. Culleton, R. Coull, R. Lupoi, G. O'Donnell, D. Trimble, Optimisation of process parameters to address fundamental challenges during selective laser melting of Ti-6Al-4V: a review, *Int. J. Mach. Tool Manu* 128 (2018) 1–20, <https://doi.org/10.1016/j.ijmactools.2018.01.003>.
- [2] D. Sun, D. Gu, K. Lin, J. Ma, W. Chen, J. Huang, X. Sun, M. Chu, Selective laser melting of titanium parts: Influence of laser process parameters on macro- and microstructures and tensile property, *Powder Technol.* 342 (2019) 371–379, <https://doi.org/10.1016/j.powtec.2018.09.090>.
- [3] S. Sun, M. Brandt, M. Easton, Powder bed fusion processes: an overview, in: *Laser Additive Manufacturing: Materials, Design, Technologies, and Applications*, 2017: pp. 55–77. 10.1016/b978-0-08-100433-3.00002-6.
- [4] D. Herzog, V. Seyda, E. Wycisk, C. Emmelmann, Additive manufacturing of metals, *Acta Mater.* 117 (2016) 371–392, <https://doi.org/10.1016/j.actamat.2016.07.019>.
- [5] C. Emmelmann, D. Herzog, J. Kranz, Design for laser additive manufacturing, *Laser Additive Manufacturing: Materials Design, Technologies, and Applications* (2017) 259–279, <https://doi.org/10.1016/b978-0-08-100433-3.00010-5>.
- [6] M. Alsaiddah, A. Khan, K. Groom, K. Mumtaz, Diode area melting of Ti6Al4V using 808 nm laser sources and variable multi-beam profiles, *Mater. Des.* 215 (2022) 110518, <https://doi.org/10.1016/j.matdes.2022.110518>.
- [7] M. Alsaiddah, A. Khan, K. Groom, K. Mumtaz, Use of 450-808 nm diode lasers for efficient energy absorption during powder bed fusion of Ti6Al4V, *Int. J. Adv. Manuf. Technol.* 113 (2021) 2461–2480, <https://doi.org/10.1007/s00170-021-06774-4>.
- [8] H. Ali, H. Ghadbeigi, K. Mumtaz, Effect of scanning strategies on residual stress and mechanical properties of Selective Laser Melted Ti6Al4V, *Mater. Sci. Eng. A* 712 (2018) 175–187, <https://doi.org/10.1016/j.msea.2017.11.103>.
- [9] J. Jhabvala, E. Boillat, T. Antignac, R. Glardon, On the effect of scanning strategies in the selective laser melting process, *Virtual Phys. Prototyp.* 5 (2010) 99–109, <https://doi.org/10.1080/17452751003688368>.
- [10] A.K. Subramanian, A.S. Reddy, S. Mathias, A. Shrivastava, P. Raghupatruni, Influence of post-processing techniques on the microstructure, properties and surface integrity of AlSiMg alloy processed by laser powder bed fusion technique, *Surf. Coat. Technol.* 425 (2021) 127679, <https://doi.org/10.1016/j.surfcoat.2021.127679>.
- [11] M.F. Sadali, M.Z. Hassan, F. Ahmad, H. Yahaya, Z.A. Rasid, Influence of selective laser melting scanning speed parameter on the surface morphology, surface roughness, and micropores for manufactured Ti6Al4V parts, *J. Mater. Res.* 35 (2020) 2025–2035, <https://doi.org/10.1557/jmr.2020.84>.

- [12] J. Gong, K. Wei, M. Liu, W. Song, X. Li, X. Zeng, Microstructure and mechanical properties of AlSi10Mg alloy built by laser powder bed fusion/direct energy deposition hybrid laser additive manufacturing, *Addit. Manuf.* 59 (2022) 103160, <https://doi.org/10.1016/j.addma.2022.103160>.
- [13] A. Jiménez, P. Bidare, H. Hassanin, F. Tarlochan, S. Dimov, K. Essa, Powder-based laser hybrid additive manufacturing of metals: a review, *Int. J. Adv. Manuf. Technol.* 114 (2021) 63–96, <https://doi.org/10.1007/s00170-021-06855-4>.
- [14] M. Zavala-Arredondo, N. Boone, J. Willmott, D.T.D. Childs, P. Ivanov, K.M. Groom, K. Mumtaz, Laser diode area melting for high speed additive manufacturing of metallic components, *Mater. Des.* 117 (2017) 305–315, <https://doi.org/10.1016/j.matdes.2016.12.095>.
- [15] C. Zhong, J. Liu, T. Zhao, T. Schopphoven, J. Fu, A. Gasser, J.H. Schleifenbaum, Laser metal deposition of Ti6Al4V—a brief review, *Appl. Sci.* 10 (2020) 764, <https://doi.org/10.3390/app10030764>.
- [16] S. Liu, Y.C. Shin, Additive manufacturing of Ti6Al4V alloy: a review, *Mater. Des.* 164 (2019) 107552, <https://doi.org/10.1016/j.matdes.2018.107552>.
- [17] W.M. Steen, J. Mazumder, *Laser Material Processing*, 4th ed., 2010. 10.1007/978-1-84996-062-5.
- [18] T. Vilario, C. Colin, J.D. Bartout, As-fabricated and heat-treated microstructures of the Ti-6Al-4V alloy processed by selective laser melting, *Met. Mater. Trans. A* 42 (2011) 3190–3199, <https://doi.org/10.1007/s11661-011-0731-y>.
- [19] S.S. Al-Bermiani, M.L. Blackmore, W. Zhang, I. Todd, The origin of microstructural diversity, texture, and mechanical properties in electron beam melted Ti-6Al-4V, *Met. Mater. Trans. A* 41 (2010) 3422–3434, <https://doi.org/10.1007/s11661-010-0397-x>.
- [20] W. Xu, M. Brandt, S. Sun, J. Elambasseril, Q. Liu, K. Latham, K. Xia, M. Qian, Additive manufacturing of strong and ductile Ti-6Al-4V by selective laser melting via in situ martensite decomposition, *Acta Mater.* 85 (2015) 74–84, <https://doi.org/10.1016/j.actamat.2014.11.028>.
- [21] S. Dai, H. Liao, H. Zhu, X. Zeng, The mechanism of process parameters influencing the AlSi10Mg side surface quality fabricated via laser powder bed fusion, *Rapid Prototyp. J.* 28 (2022) 514–524, <https://doi.org/10.1108/rpj-11-2020-0266>.
- [22] A.E. Hassanin, F. Napolitano, C. Trimarco, E. Manco, F. Scherillo, D. Borrelli, A. Caraviallo, A. Squillace, A. Astarita, Laser-powder bed fusion of Inconel 718 alloy: effect of the contour strategy on surface quality and sub-surface density, *Key Eng. Mater.* 926 (2022) 280–287, <https://doi.org/10.4028/p-u9ydc>.
- [23] M. Zavala-Arredondo, K.M. Groom, K. Mumtaz, Diode area melting single-layer parametric analysis of 316L stainless steel powder, *Int. J. Adv. Manuf. Technol.* 94 (2018) 2563–2576, <https://doi.org/10.1007/s00170-017-1040-4>.
- [24] M. Zavala-Arredondo, H. Ali, K.M. Groom, K. Mumtaz, Investigating the melt pool properties and thermal effects of multi-laser diode area melting, *Int. J. Adv. Manuf. Technol.* 97 (2018) 1383–1396, <https://doi.org/10.1007/s00170-018-2038-2>.
- [25] H. Caglar, A. Liang, K. Groom, K. Mumtaz, Multi-laser powder bed fusion of Ti6Al4V: diode area melting utilizing low-power 450 nm diode lasers, *J. Mater. Process. Technol.* 325 (2024) 118303, <https://doi.org/10.1016/j.jmatprotec.2024.118303>.
- [26] T. Ahmed, H.J. Rack, Phase transformations during cooling in  $\alpha+\beta$  titanium alloys, *Mater. Sci. Eng.: A* 243 (1998) 206–211, [https://doi.org/10.1016/s0921-5093\(97\)00802-2](https://doi.org/10.1016/s0921-5093(97)00802-2).
- [27] B. Vrancken, L. Thijs, J.-P. Kruth, J.V. Humbeeck, Heat treatment of Ti6Al4V produced by selective laser melting: microstructure and mechanical properties, *J. Alloy. Compd.* 541 (2012) 177–185, <https://doi.org/10.1016/j.jallcom.2012.07.022>.
- [28] G. Lütjering, Influence of processing on microstructure and mechanical properties of  $(\alpha+\beta)$  titanium alloys, *Mater. Sci. Eng.: A* 243 (1998) 32–45, [https://doi.org/10.1016/s0921-5093\(97\)00778-8](https://doi.org/10.1016/s0921-5093(97)00778-8).
- [29] N. Stefanoson, S.L. Semiatin, D. Eylon, The kinetics of static globularization of Ti-6Al-4V, *Met. Mater. Trans. A* 33 (2002) 3527–3534, <https://doi.org/10.1007/s11661-002-0340-x>.
- [30] L. Facchini, E. Magalini, P. Robotti, A. Molinari, Microstructure and mechanical properties of Ti-6Al-4V produced by electron beam melting of pre-alloyed powders, *Rapid Prototyp. J.* 15 (2009) 171–178, <https://doi.org/10.1108/13552540910960262>.
- [31] H. Galarraga, R.J. Warren, D.A. Lados, R.R. Dehoff, M.M. Kirka, Fatigue crack growth mechanisms at the microstructure scale in as-fabricated and heat treated Ti-6Al-4V ELI manufactured by electron beam melting (EBM), *Eng. Fract. Mech.* 176 (2017) 263–280, <https://doi.org/10.1016/j.engfracmech.2017.03.024>.
- [32] J.S. Zhang, Y.T. Tang, R. Jin, A. Lui, P.S. Grant, E. Alabort, A.C.F. Cocks, R.C. Reed, On the size-dependent fatigue behaviour of laser powder bed fusion Ti-6Al-4V, *Addit. Manuf.* 79 (2024) 103922, <https://doi.org/10.1016/j.addma.2023.103922>.
- [33] L.C. Capozzi, A. Sivo, E. Bassini, Powder spreading and spreadability in the additive manufacturing of metallic materials: a critical review, *J. Mater. Process. Technol.* 308 (2022) 117706, <https://doi.org/10.1016/j.jmatprotec.2022.117706>.
- [34] A.K. Singla, M. Banerjee, A. Sharma, J. Singh, A. Bansal, M.K. Gupta, N. Khanna, A. S. Shahi, D.K. Goyal, Selective laser melting of Ti6Al4V alloy: process parameters, defects and post-treatments, *J. Manuf. Process.* 64 (2021) 161–187, <https://doi.org/10.1016/j.jmapro.2021.01.009>.
- [35] W. Xu, E.W. Lui, A. Pateras, M. Qian, M. Brandt, In situ tailoring microstructure in additively manufactured Ti-6Al-4V for superior mechanical performance, *Acta Mater.* 125 (2017) 390–400, <https://doi.org/10.1016/j.actamat.2016.12.027>.
- [36] C. Additive, PowderRange Ti64 Datasheet, (2020). <https://www.carpenterotechnology.com/alloy-finder/powder-range-ti64> (accessed January 20, 2024).
- [37] R.W. McVey, R.M. Melnychuk, J.A. Todd, R.P. Martukanitz, Absorption of laser irradiation in a porous powder layer, *J. Laser Appl.* 19 (2007) 214–224, <https://doi.org/10.2351/1.2756854>.
- [38] S. Pal, N. Gubeljak, R. Hudák, G. Lojen, V. Rajúková, T. Brajlíh, I. Drstvenšek, Evolution of the metallurgical properties of Ti-6Al-4V, produced with different laser processing parameters, at constant energy density in selective laser melting, *Results Phys.* 17 (2020), <https://doi.org/10.1016/j.rinp.2020.103186>.
- [39] Z. Chen, X. Wu, D. Tomus, C.H.J. Davies, Surface roughness of selective laser melted Ti-6Al-4V alloy components, *Addit. Manuf.* 21 (2018) 91–103, <https://doi.org/10.1016/j.addma.2018.02.009>.
- [40] U.S. Bertoli, G. Guss, S. Wu, M.J. Matthews, J.M. Schoenung, In-situ characterization of laser-powder interaction and cooling rates through high-speed imaging of powder bed fusion additive manufacturing, *Mater. Des.* 135 (2017) 385–396, <https://doi.org/10.1016/j.matdes.2017.09.044>.
- [41] Q. Gaillard, X. Boulmat, S. Cazottes, S. Dancette, C. Desrayaud, Strength/ductility trade-off of laser powder bed fusion Ti-6Al-4V: synergetic effect of alpha-phase formation and microstructure evolution upon heat treatments, *Addit. Manuf.* 76 (2023) 103772, <https://doi.org/10.1016/j.addma.2023.103772>.
- [42] J. Yang, H. Yu, J. Yin, M. Gao, Z. Wang, X. Zeng, Formation and control of martensite in Ti-6Al-4V alloy produced by selective laser melting, *Mater. Des.* 108 (2016) 308–318, <https://doi.org/10.1016/j.matdes.2016.06.117>.
- [43] B.T. Gates-Rector, 04-020-7055, the powder diffraction file: a quality materials characterization database, *Powder Diffr.* (2019) 352–360, <https://doi.org/10.1017/s0885715619000812>.
- [44] S. Gates-Rector, Blanton, 00-044-1294, The Powder Diffraction File: A Quality Materials Characterization Database, *Powder Diffr.* (2019) 352–360. 10.1017/s0885715619000812.
- [45] A. Borbély, A. Aoufi, D. Becht, X-ray methods for strain energy evaluation of dislocated crystals, *J. Appl. Cryst.* 56 (2023) 254–262, <https://doi.org/10.1107/s1600576722012262>.
- [46] L. Owen, Powder Refinement - opening the black box, in: *Proc. 5th Int. Work. OpenCL*, The University of Sheffield, 2022; pp. 1–20.
- [47] Z. Xiao, C. Chen, Z. Hu, H. Zhu, X. Zeng, Effect of rescanning cycles on the characteristics of selective laser melting of Ti6Al4V, *Opt. Laser Technol.* 122 (2020) 105890, <https://doi.org/10.1016/j.optlastec.2019.105890>.
- [48] X.-J. Shen, C. Zhang, Y.-G. Yang, L. Liu, On the microstructure, mechanical properties and wear resistance of an additively manufactured Ti64/metallic glass composite, *Addit. Manuf.* 25 (2019) 499–510, <https://doi.org/10.1016/j.addma.2018.12.006>.
- [49] Data Sheet - Ti6al4v carpenter grade 23 powder, (n.d.). [https://www.carpenteradditive.com/hubfs/Resources/Data%20Sheets/PowderRange\\_Ti64\\_Datasheet.pdf](https://www.carpenteradditive.com/hubfs/Resources/Data%20Sheets/PowderRange_Ti64_Datasheet.pdf) (accessed August 3, 2023).
- [50] G. Zhang, J. Chen, M. Zheng, Z. Yan, X. Lu, X. Lin, W. Huang, Element vaporization of Ti-6Al-4V alloy during selective laser melting, *Metals* 10 (2020) 435, <https://doi.org/10.3390/met10040435>.
- [51] J. Liu, P. Wen, Metal vaporization and its influence during laser powder bed fusion process, *Mater. Des.* 215 (2022) 110505, <https://doi.org/10.1016/j.matdes.2022.110505>.
- [52] K. Dietrich, J. Diller, S.-D.-L. Goff, D. Bauer, P. Forêt, G. Witt, The influence of oxygen on the chemical composition and mechanical properties of Ti-6Al-4V during laser powder bed fusion (L-PBF), *Addit. Manuf.* 32 (2020) 100980, <https://doi.org/10.1016/j.addma.2019.100980>.
- [53] P.A. Hooper, Melt pool temperature and cooling rates in laser powder bed fusion, *Addit. Manuf.* 22 (2018) 548–559, <https://doi.org/10.1016/j.addma.2018.05.032>.
- [54] T. DebRoy, H.L. Wei, J.S. Zuback, T. Mukherjee, J.W. Elmer, J.O. Milewski, A. M. Beese, A. Wilson-Heid, A. De, W. Zhang, Additive manufacturing of metallic components – process, structure and properties, *Prog. Mater. Sci.* 92 (2018) 112–224, <https://doi.org/10.1016/j.pmatsci.2017.10.001>.
- [55] D.A. Porter, K.E. Easterling, K.E. Easterling, *Phase Transformations in Metals and Alloys* (Revised Reprint) (2009), <https://doi.org/10.1201/9781439883570>.
- [56] S. Megahed, V. Aniko, J.H. Schleifenbaum, Electron beam-melting and laser powder bed fusion of Ti6Al4V: transferability of process parameters, *Metals* 12 (2022) 1332, <https://doi.org/10.3390/met12081332>.
- [57] R.W. Armstrong, The influence of polycrystal grain size on several mechanical properties of materials, *Met. Mater. Trans. B* 1 (1970) 1169–1176, <https://doi.org/10.1007/bf02900227>.
- [58] A. Liang, K.S. Pey, T. Polcar, A.R. Hamilton, Effects of rescanning parameters on densification and microstructural refinement of 316L stainless steel fabricated by laser powder bed fusion, *J. Mater. Process. Technol.* 302 (2022) 117493, <https://doi.org/10.1016/j.jmatprotec.2022.117493>.
- [59] A. Pathania, A.K. Subramanian, B.K. Nagesha, Influence of post-heat treatments on microstructural and mechanical properties of LPBF-processed Ti6Al4V alloy, *Prog. Addit. Manuf.* 7 (2022) 1323–1343, <https://doi.org/10.1007/s40964-022-00306-6>.
- [60] R. Shi, S.A. Khairallah, T.T. Roehling, T.W. Heo, J.T. McKeown, M.J. Matthews, Microstructural control in metal laser powder bed fusion additive manufacturing using laser beam shaping strategy, *Acta Mater.* 184 (2020) 284–305, <https://doi.org/10.1016/j.actamat.2019.11.053>.
- [61] S.Q. Wu, Y.J. Lu, Y.L. Gan, T.T. Huang, C.Q. Zhao, J.J. Lin, S. Guo, J.X. Lin, Microstructural evolution and microhardness of a selective-laser-melted Ti-6Al-4V alloy after post heat treatments, *J. Alloy. Compd.* 672 (2016) 643–652, <https://doi.org/10.1016/j.jallcom.2016.02.183>.